COMMUNICATIONS PHYSICS

ARTICLE

https://doi.org/10.1038/s42005-019-0221-x OPEN

Reconfigurable flows and defect landscape of confined active nematics

Jérôme Hardoüin[1,2,7], Rian Hughes[3,7], Amin Doostmohammadi[3], Justine Laurent[4,5], Teresa Lopez-Leon[6], Julia M. Yeomans[3*], Jordi Ignés-Mullol[1,2*] & Francesc Sagués[1,2]

The physics of active liquid crystals is mostly governed by the interplay between elastic forces that align their constituents, and active stresses that destabilize the order with constant nucleation of topological defects and chaotic flows. The average distance between defects, also called active length scale, depends on the competition between these forces. Here, in experiments with the microtubule/kinesin active nematic system, we show that the intrinsic active length scale loses its relevance under strong lateral confinement. Transitions are observed from chaotic to vortex lattices and defect-free unidirectional flows. Defects, which determine the active flow behaviour, are created and annihilated on the channel walls rather than in the bulk, and acquire a strong orientational order in narrow channels. Their nucleation is governed by an instability whose wavelength is effectively screened by the channel width. These results are recovered in simulations, and the comparison highlights the role of boundary conditions.

[1] Departament de Química Física, Universitat de Barcelona, 08028 Barcelona, Spain. [2] Institute of Nanoscience and Nanotechnology, Universitat de Barcelona, 08028 Barcelona, Spain. [3] The Rudolf Peierls Centre for Theoretical Physics, Clarendon Laboratory, Parks Road, Oxford OX1 3PU, UK. [4] Laboratoire de Physique et Mécanique des Milieux hétérogènes (PMMH), UMR CNRS 7636, ESPCI Paris, PSL Research University, Paris, France. [5] Sorbonne Université, Univ. Paris Diderot, Paris, France. [6] Laboratoire Gulliver, UMR CNRS 7083, ESPCI Paris, PSL Research University, Paris, France. [7] These authors contributed equally: Jérôme Hardoüin, Rian Hughes *email: julia.yeomans@physics.ox.ac.uk; jignes@ub.edu

Active matter refers to systems composed of self-driven units, such as tissues, bacterial suspensions, or mixtures of biofilaments and motor proteins, that organise their textures and flows autonomously by consuming either stored or ambient free energy[1,2]. This distinctive hallmark sometimes conceals another significant, and often unappreciated, feature of active systems: their capability to adapt to the environments where they reside. For example, human cancer cells switch between distinct invasion modes when they encounter constrictions in the crowded environment of stroma[3], and the growth of bacterial biofilms can be directed by their surroundings[4]. Moreover, geometrical confinement tends to control active flows, replacing the bulk chaotic flow state often termed active turbulence, by more regular flow configurations. Understanding the subtleties of how this occurs will have relevance to possible future applications of active materials in microfluidics and self-assembly, and in assessing the relevance of the concepts of active matter in the description of biological systems.

Recent contributions dealing with confinement in bacterial suspensions and cell layers have demonstrated a rich range of behaviour. Competition between wall orientation, hydrodynamic interactions, topology and activity lead to a wide variety of flow patterns: spiral vortices[5,6], synchronised vortex lattices[7], unidirectional flows[8–10], shear flows[11] and freezing[12,13]. Work on confining active mixtures of microtubules and motor proteins to circular domains[14–17], in vesicles[18] or droplets[19,20] and to more complex geometries such as tori[21,22], have already probed the specific effects of interfacial viscosity, curvature and 3D confinement. These experimental results have prompted parallel simulations[23–28].

Here we concentrate on active nematics confined to two-dimensional channels. The system is composed of self-propelling elongated units formed by bundled microtubules powered by adenosine triphosphate (ATP)-consuming kinesin[29]. Early theoretical work predicted that laterally-confined active nematics undergo an instability to spontaneous laminar flow when the channel width reaches a typical length scale that depends on the strength of the activity[30]. This prediction has been recently confirmed in experiments with spindle-shaped cells[11]. On the other hand, simulations have predicted that, at higher activities or in wider channels, a structured 'dancing' state can be stable in active nematics[31]. Our aim here is to assess, in a well-controlled and tunable experimental system, and with the support of numerical simulations, the role of confinement in the patterns and dynamics of an active nematic. In particular, we explore the emergence of a new length scale different from the active length that characterizes the unconfined systems. We find a rich dynamical behaviour, depending on the channel width. More specifically, we uncover a defect-free regime of shear flow in narrow channels. This regime is unstable with respect to the nucleation of short-lived defects at the walls. By increasing the channel width, defect lifetime increases, developing a spatio-temporal organization that corresponds to the predicted state of dancing vortical flows[31], before full disorganization into the active turbulence regime for still wider channels, as is typical of the unconfined active nematic. We stress the close interplay between the velocity field and the defect dynamics, and highlight the emergence of a new length scale that, contrary to the classical active length scale, does not depend on the activity level but merely on geometrical parameters.

Results

Experimental setup. The active system we use comprises microtubules powered by ATP-consuming, two headed kinesin molecular motors[29]. Addition of the depleting agent polyethylene glycol (PEG) concentrates the microtubules into bundles, hundreds of microns long. Within each bundle the kinesin motors bridge neighbouring microtubules and walk towards their positive ends leading to internal sliding of filaments of opposite polarity. The active nematic was prepared using an open-cell design[32], in which 2 μL of the active aqueous microtubule-mixture was placed inside a custom-made pool of 5 mm diameter and was covered with 60 μL of 100 cSt silicon oil (see Methods). Within 30 min, an active nematic layer extends over the whole surface of the pool. Driven by the motors, the microtubule bundles at the interface continuously extend and buckle. This gives rise to a dynamical steady state, termed active turbulence, characterised by high vorticity and by the creation, translation and destruction of topological defects.

The layer of active nematic is confined in rectangular enclosures by means of micro-printed polymer grids of 100 μm thickness that are placed in contact with the oil/aqueous interface (see Fig. 1a). The active nematic is in contact with the active bulk solution underneath, thus ensuring activity and material parameters are equal in all channels. A detailed sketch of the experimental protocol is available in Supplementary Fig. 1.

Computational setup. To model the dynamics of the confined microtubule-motor system we use a continuum description of a two-dimensional, active gel[1,2,33,34]. The fields that describe the system are the total density ρ, the velocity $\boldsymbol{u}$, and the nematic tensor $\mathbf{Q} = 2q(\mathbf{nn} - \mathbf{I}/2)$, that describes both the orientation ($\mathbf{n}$) and the magnitude (q) of alignment of the nematogens.

The nematic tensor is evolved according to the Beris–Edwards equation[35]

$$(\partial_t + \boldsymbol{u}\cdot\boldsymbol{\nabla})\mathbf{Q} - \mathbf{S} = \Gamma_Q \mathbf{H}, \tag{1}$$

where $\mathbf{S} = \xi\mathbf{E} - (\boldsymbol{\Omega}\cdot\mathbf{Q} - \mathbf{Q}\cdot\boldsymbol{\Omega})$ is a generalised advection term, characterising the response of the nematic tensor to velocity gradients. Here, $\mathbf{E} = (\nabla\boldsymbol{u} + \nabla\boldsymbol{u}^{\mathrm{T}})/2$ is the strain rate tensor, $\boldsymbol{\Omega} = (\nabla\boldsymbol{u}^{T} - \nabla\boldsymbol{u})/2$ the vorticity tensor, and ξ is the alignment parameter representing the collective response of the microtubules to velocity gradients. Γ_Q is a rotational diffusivity and the molecular field $\mathbf{H} = -\frac{\delta\mathcal{F}}{\delta\mathbf{Q}} + \frac{\mathbf{I}}{2}\mathrm{Tr}\left(\frac{\delta\mathcal{F}}{\delta\mathbf{Q}}\right)$, models the relaxation of the orientational order to minimise a free energy $\mathcal{F}$.

The free energy includes two terms. The first is an elastic free energy density, $\frac{1}{2}K(\boldsymbol{\nabla}\mathbf{Q})^2$, which penalises any deformations in the orientation field of the nematogens and where we assume a single elastic constant K. We note that the free energy functional does not include any Landau-de Gennes bulk free energy terms: all the ordering in the simulations arises from the activity[36]. This is motivated by the fact that there is no equilibrium nematic order in the experimental system without ATP (i.e., in the absence of active driving). The second contribution to the free energy is a surface anchoring, $\frac{1}{2}W\mathrm{Tr}(\mathbf{Q} - \mathbf{Q}_{\mathrm{D}})^2$. To correspond to the experiments $\mathbf{Q}_{\mathrm{D}}$ is chosen so that the director prefers to align parallel to the boundary walls. The strength of anchoring at the boundaries, W, is set to values corresponding to weak anchoring so that the nematogens can re-orientate at the walls to allow defects to form there.

The total density ρ satisfies the continuity equation and the velocity $\mathbf{u}$ evolves according to

$$\rho(\partial_t + \boldsymbol{u}\cdot\boldsymbol{\nabla})\boldsymbol{u} = \boldsymbol{\nabla}\cdot\boldsymbol{\Pi}, \tag{2}$$

where $\boldsymbol{\Pi}$ is the stress tensor. The stress contributions comprise the active stress $\boldsymbol{\Pi}^{\mathrm{active}} = -\zeta\mathbf{Q}$ where ζ is the activity coefficient, viscous stress $\boldsymbol{\Pi}^{\mathrm{viscous}} = 2\eta\mathbf{E}$, where η is the viscosity, and the elastic stresses $\boldsymbol{\Pi}^{\mathrm{elastic}} = -P\mathbf{I} - 2\xi q\mathbf{H} + \mathbf{Q}\cdot\mathbf{H} - \mathbf{H}\cdot\mathbf{Q} - \boldsymbol{\nabla}\mathbf{Q}\frac{\delta\mathcal{F}}{\delta\boldsymbol{\nabla}\mathbf{Q}}$, where $P = p - \frac{K}{2}(\boldsymbol{\nabla}\mathbf{Q})^2$ is the modified pressure. Equations (1)

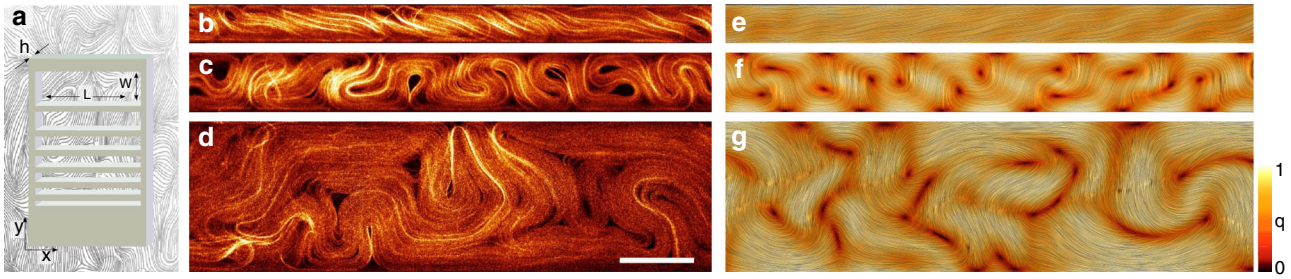

Fig. 1 Flow states. **a** Top view of the experimental setup including the relevant spatial dimensions. A polymer plate with rectangular openings is placed, by means of a micropositioner, at the interface between the active fluid and silicon oil, thus constraining the existing active nematic. **b**–**d** Confocal fluorescence micrographs of an active nematic interface confined in channels of different widths. Scale bar: 100 μm. **e**–**g** Corresponding simulations of the experimental system. Streaking patterns follow the director field tangents. They are produced using a Line Integral Convolution of the director field[56] with Paraview software.The colour map corresponds to the computed nematic order parameter, *q*. **b**, **e** Correspond to strong confinement, where the filaments are organized into a unstable shear alignment regimee. **c**, **f** Illustrate the effects of moderate confinement, forcing a new dynamical regime of the defects. **d**, **g** Correspond to the active turbulence regime

and (2) were solved numerically using a hybrid lattice–Boltzmann method[37,38]. In the experiments the microtubules slide over the walls and therefore free-slip boundary condition were imposed on the velocity field. See Methods for simulation parameters.

Flow states. The main experimental control parameters of our system are the channel width, w, and the concentration of ATP, which determines the activity. In this section, we describe how both the defect landscape and flow patterns evolve as w is increased based on experiments (Fig. 1b–d) and simulations (Fig. 1e–g). We identify two well-defined regimes: a shear flow regime, observed for $w < 80\,\mu$m, which is transiently defect-free (Fig. 1b, e, and Supplementary Movies 1–3), and the dancing defects regime, for $w > 90\,\mu$m (Fig. 1c, f, and Supplementary Movies 4 and 5). The transition between these two regimes is not sharp. For values of w in the range 80−90 μm, the direction of the shear is not uniform along the channel, but rather composed of patchy domains where shear flow spontaneously arises with a random direction, and is then quickly disrupted by instabilities (see Supplementary Movies 6 and 7). Finally, the unconfined active nematics is obtained for $w > 120\,\mu$m (Fig. 1d, g).

We find that the relevant parameter setting the dynamic state in the system is λ/w, where λ is the mean defect separation (Fig. 2). The latter is defined as $\lambda = (Lw/N)^{1/2}$, where L is the length of a given channel, w its width, and N the number of defects averaged in time. For unconfined active nematics, this length scale coincides with $l_a = \sqrt{K/\zeta}$, often referred to as the active length-scale, which determines the vortex size distribution and corresponds to the mean defect separation[14,38,39]. However, we find that, in confined active nematics, λ is no longer equal to l_a. Instead, it significantly decreases with the channel width (see Supplementary Fig. 2).

In the following, the flow dynamics and the defect landscape are analysed, combining experiments and simulations, for the simple shear (Fig. 3a), flow switching (Fig. 3b), and defect dancing (Fig. 3c) regimes.

Defect-free shear flow disrupted by instabilities. The shear flow regime is a defect-free state that appears for $\lambda/w > 1$ (Fig. 2), experimentally realized here for $w < 80\,\mu$m. The active material is primarily aligned parallel to the walls over distances that can persist along the whole channel as shown in Fig. 3a. A global shear deformation is observed, with flows along the channel (Supplementary Fig. 3). The maximum velocities are measured at the walls, with opposite signs, and the velocity perpendicular to

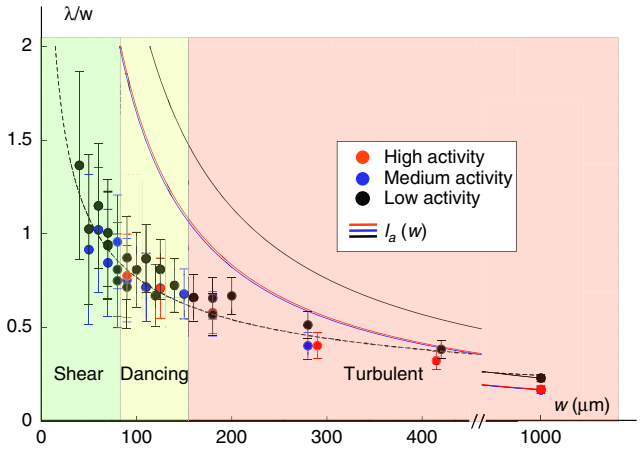

Fig. 2 Defect Spacing. Experimental mean defect spacing, λ, rescaled by the channel width, w, as a function of w. Different colours correspond to different activities. The error bars correspond to the standard deviation for measurements at 10 random times for each experiment. The non-scaled data is displayed in Supplementary Fig. 2. The dotted line corresponds to a fit with $w^{-1/2}$. The continuous lines correspond to $\lambda/w = l_a/w$ for each experiment, with l_a being the active length scale corresponding to the value of λ in the unconfined case

the walls is negligible. The shear rate, characterised by the slope of the velocity profile, is approximately constant over a relatively large range of channel widths. This is as expected because the activity, and hence the energy input per unit area, which must be balanced by the viscous dissipation due to the shear, is the same for all channels.

This aligned, defect-free configuration shares visual similarities with the banding patterns that emerge in simulations of dry systems of self-propelled particles with nematic alignment[40,41]. A fundamental difference with our system, which is continuous rather than composed of discrete particles, is the fact that, in our case, nematic order in intrinsic, and flow alignment is the result of hydrodynamic and elastic interactions with the boundaries. In contrast, in the mentioned dry systems, nematic order is restricted to bands that arise from giant density fluctuations allowed by the compressible nature of the particle ensembles.

Extensile active nematics, such as the one that we use here, are intrinsically unstable to bend deformations[30,42–44] in aligned conformations. As a consequence, the sheared state eventually

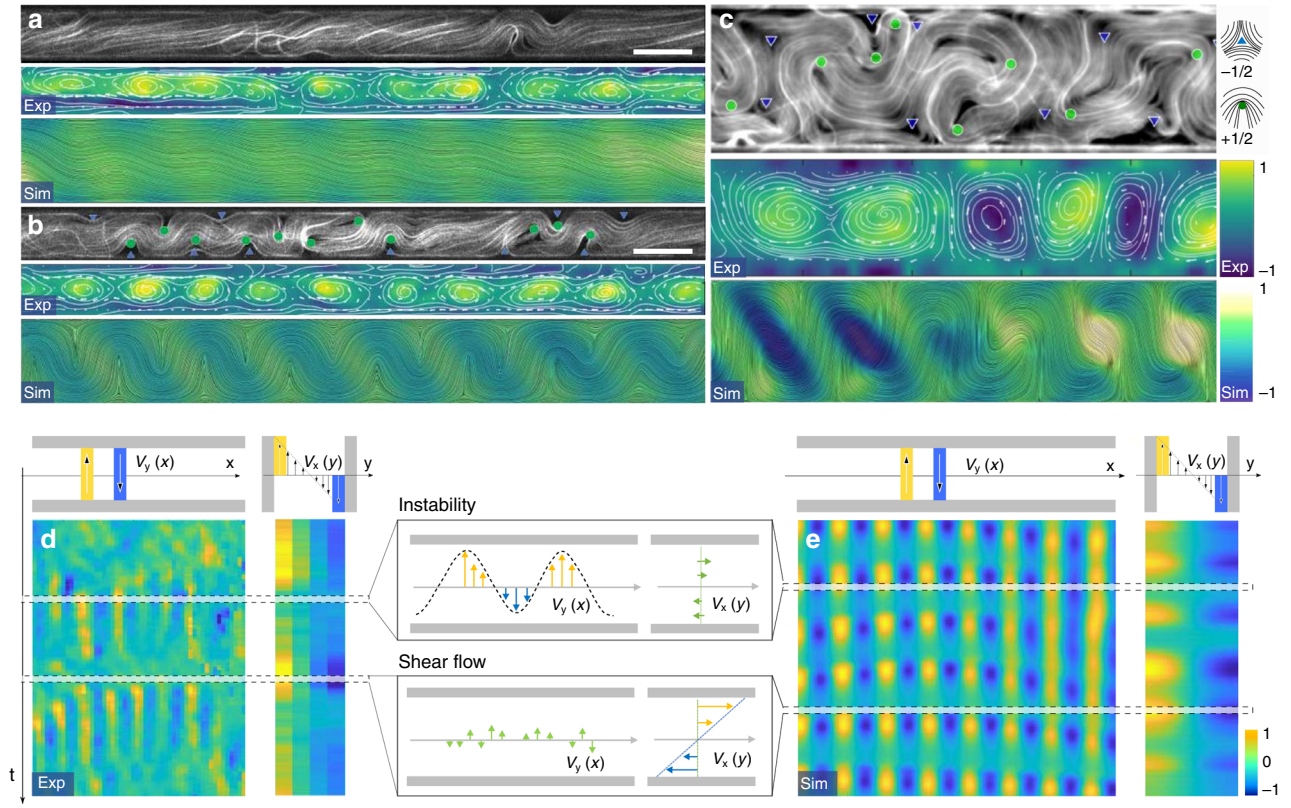

Fig. 3 Flow patterns and periodic instabilities in the shear state. **a**–**d** Each panel is composed of (top) a snapshot of a typical confocal fluorescence image of the active nematic, with defect locations overlaid, (center) experimental Particle Image Velocimetry measurement of the flow patterns, coloured by the normalized vorticity, with velocity streamlines overlaid and (bottom) numerical simulations coloured by the normalized vorticity. Lines in the simulations correspond to the director field. **a** Shear flow state, $\lambda/w \sim 1$, in the shear phase. **b** Shear flow state, $\lambda/w \sim 1$, in the instability phase. **c** Dancing state, $\lambda/w \sim 0.7$. Scale bars: 50 μm. **d**, **e** Experimental kymographs for V_x averaged along the channel and V_y averaged across the channel are shown in **d** while the corresponding simulations appear in **e**. The colour encodes the normalized velocity components. One instance of stable shear flow regime and one instance of transversal instability are sketched

leads to local bend instabilities as shown in Fig. 3b. As a result, the velocity field repeatedly switches between two different states: longitudinal shear flow and a transversal instability regime (see Supplementary Movies 1 and 2). The dynamics of the switching behaviour and the coexistence of the shear and the instability states can be best illustrated in a space-time diagram of the averaged velocity components in the channel, as shown in Fig. 3d, e. In the shear state, the velocity perpendicular to the boundaries and averaged across the channel width, $\langle V_y(x)\rangle_y$, vanishes, while the velocity component parallel to the channel walls and averaged along the channel length, $\langle V_x(y)\rangle_x$, is maximum at the walls. Once bend instabilities are triggered, defect pairs form and +1/2 defects propagate across the channel and dismantle the shear state, which leads to the emergence of non-zero values of $\langle V_y(x)\rangle_y$ with a well-defined length scale along the channel. The defects eventually reach the opposing wall and annihilate, such that the shear state is reestablished. As is apparent from Fig. 3d, e, over time the active system alternates between the two regimes. Simulations allowed to test channel widths well below the experimental capabilities, allowing to explore the $\lambda \gg w$ regime. For these conditions, we observed stable shear flow, as any pairs of defects that were generated at the channel walls immediately self-annihilated (see Supplementary Movie 8).

The instability takes the form of a sinusoidal deformation of the aligned nematic field, with a well-defined length-scale along the channel. As the perturbation progresses, defects are rapidly nucleated from the walls, at regularly-spaced positions coinciding with the maxima of the sinusoidal perturbation. We measured the wavelength of the instability and found that it scales with the channel width (Fig. 4a–c). This is strong evidence that the hydrodynamics is screened, and that the channel width is important in controlling the flows.

Upon their nucleation at the boundaries, the orientation of the +1/2 defects is strongly anisotropic (see Fig. 5a). They preferentially align perpendicular to the walls and, due to their active self-propulsion[25,29,45], they move away from the walls into the bulk. On the contrary, because of their three-fold symmetric configuration, −1/2 defects have no self-propulsion and remain in the vicinity of the walls[31]. Eventually, the +1/2 defects reach the opposite wall and annihilate with negative defects residing close to it. In this way, the defect-free phase is periodically restored (see Supplementary Movie 3). Remarkably, even though no chirality is observed in the sheared state, as we repeat the experiments, the handedness of the shear flow initially selected is preserved through successive instability cycles. This memory can be explained by observing that the instability is triggered locally and that it is entrained by the neighbouring sheared regions.

In a recent paper Opathalage et al.[17] have reported similar defect nucleation at the boundaries for a microtubule/kinesin mixture in circular confinement with no-slip boundary conditions and planar anchoring. They attribute the rate of defect formation to a combination of the build-up of microtubule density at the boundary increasing local active stresses and a change in the azimuthal force as circular flows wind the microtubules around the confining disk. In our experiments and simulations variation of microtubule density across the

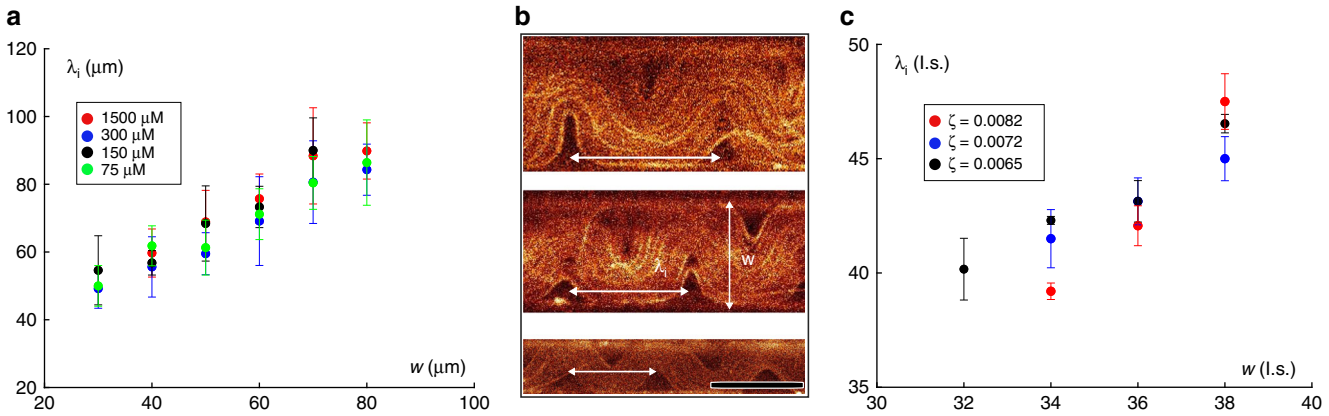

Fig. 4 Instability wavelength. **a** Measurement of the instability wavelength λ_i vs w for different values of activity, controlled by the adenosine triphosphate concentration, whose values are displayed in the legend. **b** Fluorescent micrographs displaying the measurement of the instability wavelength λ_i at the onset of defect nucleation in the shear state for three different channels widths w. λ_i is taken as the distance between two neighbouring negative defects along a given wall, as indicated. Scale bar: 50 μm. **c** λ_i vs w in simulations, for different values of activity as indicated. The unit of the axes is the number of lattice sites (l.s.). In **a** error bars correspond to the standard deviation of the measurements for about 10 independent instability onsets per channel. In **c** error bars correspond to the standard deviation of the measurements

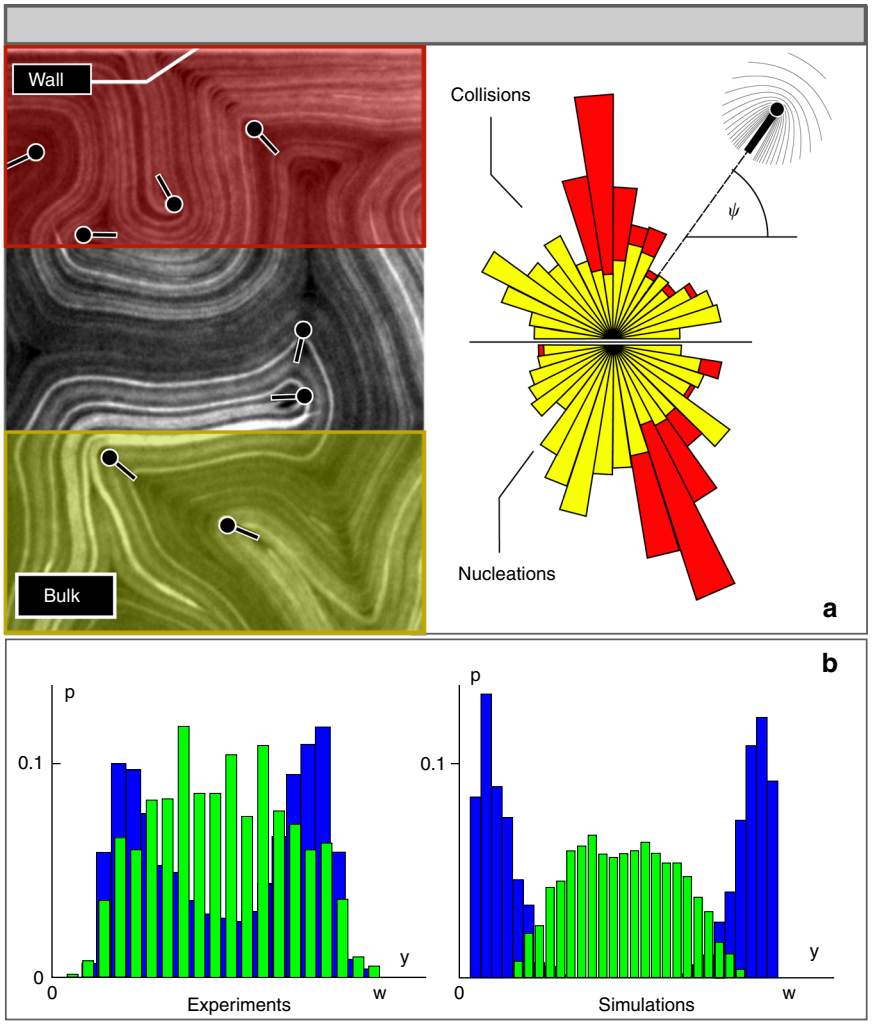

Fig. 5 Defect nucleation. **a** Statistical distribution of positive defect orientations. The angle ψ corresponds to the orientation of the defect with respect to the wall. $\psi = \pi/2$ (resp. $\psi = 3\pi/2$) corresponds to a defect perpendicularly colliding with (resp. moving away from) the wall. The red distribution is the result for defects close to the wall, while the yellow distribution refers to bulk defects. **b** Experimental (left) and simulated (right) probability distributions of defect position across a channel. Green (blue) distribution refers to positive (negative) defects

channel is small (except in defect cores) and the instability period is controlled by the time taken to realign the microtubules parallel to the walls after each instability. This realignement period not only decreases significantly for increasing channel width, but also for increasing activity as shown in Supplementary Fig. 4.

The dancing state: a one-dimensional line of flow vortices. Increasing the channel width to values between 90 and 120 μm, one-dimensional arrays of vortices are observed as shown in Fig. 3c. A close look at the defect distribution reveals that the transition to the flow state with organised vorticity arrays corresponds to the point when the channel can accommodate more than one defect in its cross-section, i.e., $\lambda/w < 1$ (Fig. 2). One could expect that this criterion is reached when the channel width becomes comparable to the active length-scale. However as shown in Fig. 2, l_a/w is still much larger than 1 in the range of the dancing state, i.e., $\lambda \ll l_a$. Furthermore, contrary to the l_a/w curves, λ/w does not seem to depend on activity, supporting the idea that λ is indeed a pure geometrical feature. Dynamically, the system behaves as if two distinct populations of positive defects are travelling along the channel in opposite directions, passing around each other in a sinusoidal-like motion. A similar state had been predicted by simulations and was referred to as the dancing state[31]. However, contrary to the published simulations, the dancing state observed in our experiments is quite fragile, and vortex lattices are always transient and localised in space. Defects may annihilate with their negative counterparts, or even switch their direction of motion, thus perturbing the flow pattern (see Supplementary Movies 4 and 5). The difference between the spatial organisation of oppositely charged defects in the confined active nematic is manifest in their arrangement across the width of the channel (Fig. 5b and Supplementary Fig. 5a–c). The distribution of the +1/2 defects has a single peak at the centre of the channel (Fig. 5b, green). On the other hand, the −1/2 defect distribution has two peaks, one at each of the boundary walls (Fig. 5b, blue) and the profiles do not rescale with the channel width. Instead, the wall-peak distance is approximately constant at a separation ~18 μm from the wall, as shown in Supplementary Fig. 5d. This can be attributed to −1/2 defects having no self-propulsion and thus interacting elastically with the channel walls[46]. The distance of the −1/2 defect from the walls is therefore expected to be controlled by the intrinsic anchoring penetration length of the nematic $l_n = K/W$, which is set by the competition between the orientational elastic constant K and the strength of the anchoring at the wall W, and is independent of the channel width and activity of the particles. As expected, for wider channels, $w > 120\ \mu$m, the difference between the +1/2 and −1/2 defect distributions diminishes as active turbulence is established (see Supplementary Fig. 5c). We observed a similar behaviour in the simulations, but the −1/2 defects were more strongly localised near the walls, and the +1/2 defects consequently tended to lie towards the centre of the channel (Fig. 5b). Simulations have also allowed us to pinpoint the necessary boundary conditions at the channel walls to trigger defect nucleation. We find that such a localised defect formation at the walls is obtained only for free-slip boundary conditions for the velocity, and weak planar anchoring boundary conditions for the nematic director field. This is because the free-slip velocity, together with the parallel anchoring of the director, allows for strong tangential active flows, and hence strong tangential nematic order, to develop along the boundaries. This results in bend instabilities that grow perpendicular to the walls with the weak strength of the anchoring allowing the director to deviate from a planar configuration at the positions where the bend instability is developed. Our previous simulations that assumed no-slip velocity and strong alignment conditions on the confinement did not observe defect nucleation at the boundaries[31,47], and showed insensitivity of the active nematic patterns to the boundary conditions[47]. This is because the strong anchoring used in these works prevented defects forming at the walls.

It is, however, interesting to note that a recent computational study, based on a kinetic approach, has reported a special case of defect nucleation at the boundaries of an active nematic confined within a circular geometry with no-slip velocity boundary condition and free anchoring[48]. However, in that work the wall-bound defect nucleation was observed only for confining disks of small sizes and had a very different dynamics than that reported here: the +1 defect imposed by the circular geometry was first dissociated into two +1/2 defects and then, for sufficiently small confinement one of the +1/2 defects kept moving into and out of the boundary. This is in contrast to our results that show regularly-spaced defect pair nucleation sites at the boundaries for a range of channel widths. Moreover, we find that the corresponding defect spacing is governed by an instability wavelength that is no longer given by the conventional active length scale.

Discussion

We have presented experimental results, supported by continuum simulations, investigating the flow and defect configurations of an active nematic confined to rectangular channels of varying width. Our experiments have identified a new dynamical state, where well-defined shear flow alternates in a regular way with bursts of instability characterised by +1/2 topological defects moving across the channel. We have also shown that, for wider channels, it is possible to identify the dancing state[31], although the particular boundary conditions considered in the present work make it less stable.

Our work highlights the importance of topological defects in controlling the confined flows. Because the microtubules have weak planar anchoring and can freely slide along the channel walls, pairs of ±1/2 defects form at the walls of the channel. The +1/2 defects are self-propelled and move away from the walls whereas the −1/2 defects remain close to the boundaries. The distance to the boundaries is set by the anchoring penetration length. In bulk active nematics the defect spacing is set by the active length scale and, although there is some evidence of long-range ordering[49–51], defect motion is primarily chaotic. In confinement, however, the defect spacing and the wavelength of the instability are set by the channel width and the defect trajectories are more structured.

Together, experiments and simulations demonstrate a surprisingly rich topological defect dynamics in active nematics under channel confinement, and a sensitive dependence on both channel width and boundary conditions. Therefore, confinement provides a way of controlling active turbulence and defect trajectories, a pre-requisite for using active systems in microfluidic devices.

Methods

Complementary information about the preparation of active samples and grid manufacturing is given in Supplementary information, together with additional comments on image acquisition and data analysis. Details pertaining to the simulations including a table with all parameter values and a discussion on boundary conditions are also provided.

Protein preparation. Microtubules (MTs) were polymerized from heterodimeric (ζ, β)-tubulin from bovine brain [a gift from Z. Dogic's group at Brandeis University (Waltham, MA)], incubated at 37 °C for 30 min in aqueous M2B buffer (80 mM Pipes, 1 mM EGTA, 2 mM $MgCl_2$) prepared with Milli-Q water. The mixture was supplemented with the reducing agent dithiothrethiol (DTT) (Sigma; 43815) and with guanosine-5-[(ζ, β)-methyleno]triphosphate (GMPCPP)

(Jena Biosciences; NU-405), a slowly hydrolysable analogue of the biological nucleotide guanosine-5′–triphosphate (GTP) that completely suppresses the dynamic instability of the polymerized tubulin. GMPCPP enhances spontaneous nucleation of MTs, obtaining high-density suspensions of short MTs (1–2 μm). For fluorescence microscopy, 3% of the tubulin was labelled with Alexa 647. Drosophila melanogaster heavy-chain kinesin-1 K401-BCCP-6His (truncated at residue 401, fused to biotin carboxyl carrier protein (BCCP), and labelled with six histidine tags) was expressed in Escherichia coli using the plasmid WC2 from the Gelles Laboratory (Brandeis University) and purified with a nickel column. After dialysis against 500 mM imidazole aqueous buffer, kinesin concentration was estimated by means of absorption spectroscopy. The protein was stored in a 60% (wt.vol^{-1}) aqueous sucrose solution at −80 °C for future use.

Imaging. Images were acquired using a laser scanning confocal microscope Leica TCS SP2 AOBS with a 10× objective at typical frame rates of 1 image per second. For each experiment and at each time, a frame is acquired in both fluorescence and reflection mode. Fluorescence is used to visualize the nematic field, and reflection images are used for Particle Image Velocimetry (PIV) measurements as explained in the data analysis section.

Grid manufacturing. The grids are printed using a two-photon polymerization printer, a Nanoscribe GT Photonic Professional device, with a negative-tone photoresist IP-S (Nanoscribe GmbH, Germany) and a ×25 objective. The grids were directly printed on silicon substrates without any preparation to avoid adhesion of the resist to the substrate (plasma cleaning of the substrate, for example, would increase the adhesion). After developing 30 min in propylene glycol monomethyl ether acetate (PGMEA 99,5%, Sigma Aldrich) and 5 min in isopropanol (Technical, VWR), a batch polymerization is performed with UV-exposure (5 min at 80% of light power). After printing onto a silicon wafer, the grids are bound to a vertical glass capillary with a UV-curable glue. The capillary is then delicately manipulated to detach the grids from the printing support. The grids are washed in three steps (iso-propanol, DI water, ethanol) and dried with a nitrogen stream before each experiment. The thickness of the grids is 100 μm, to ensure good mechanical resistance. We have used grids with rectangular openings 1.5 mm long and widths ranging from 30 to 300 μm. Each grid contains different channel widths so that simultaneous experiments can be performed with the same active nematic preparation, thus ensuring that material parameters remain unchanged when comparing different confinement conditions. The micro-patterning has a resolution of around 50 nm, much higher than the needs of the experiment. The boundary conditions also appear to be very well defined. We never observe microtubules sticking to the wall. As shown by the flow profiles measured in the shear state, the shear profile extends up to the wall, attesting for a free slip boundary condition. The thickness of the active nematic layer is of the order of a few microns, much thinner than the grids. When the grid comes to the interface, we observe that the bound interface tends to lie somewhere in between the top and bottom of the grid, as shown in Fig. 1c. When the grid impacts the interface, uncontrolled flows may destabilize the active nematic layer. These flows mostly depend on the parallelism upon impact, but also on the wetting properties of the grid. The parallelism is relatively easy to control with micro-screw adjustment. On the other hand, the wetting properties of the grid are still under scrutiny. In our experience, the surface of the grids deteriorates after the first use, therefore the samples are considered single-use.

Active gel preparation. Biotinylated kinesin motor protein and tetrameric streptavidin (Invitrogen; 43-4301) aqueous suspensions were incubated on ice for 30 min at the specific stoichiometric ratio 2:1 to obtain kinesin–streptavidin motor clusters. MTs were mixed with the motor clusters that acted as cross-linkers, and with ATP (Sigma; A2383) that drove the activity of the gel. The aqueous dispersion contained a nonadsorbing polymeric agent (PEG, 20 kDa; Sigma; 95172) that promoted the formation of filament bundles through depletion. To maintain a constant concentration of ATP during the experiments, an enzymatic ATP-regenerator system was used, consisting on phosphoenolpyruvate (PEP) (Sigma; P7127) that fueled pyruvate kinase/lactate dehydrogenase (PK/LDH) (Invitrogen; 434301) to convert ADP back into ATP. Several antioxidant components were also included in the solution to avoid protein denaturation, and to minimize photo-bleaching during characterization by means of fluorescence microscopy. Anti-oxydant solution 1 (AO1) contained 15 mg.mL^{-1} glucose and 2.5 M DTT. Anti-oxidant solution 2 contained 10 mg.mL^{-1} glucose oxydase (Sigma G2133) and 1.75 mg.mL^{-1} catalase (Sigma, C40). Trolox (Sigma, 238813) was used as an additional antioxidant. A high-salt M2B solution was used to raise the $MgCl_2$ concentration. The PEG-based triblock copolymer surfactant Pluronic F-127 (Sigma; P-2443) was added to procure a biocompatible water/oil interface in subsequent steps. Buffer for stock solutions of PEP, DTT, ATP, PEG and Streptavidin was M2B, and we added 20 mM of K_2HPO_4 to the buffer of catalase, glucose, glucose oxydase and trolox. A typical recipe is summarized in Table 1.

Data analysis. Statistical information on defect unbinding and defect orientation (Fig. 5) were obtained using the defect detection and tracking Matlab codes developed by Ellis et al.[21,22], coupled with a custom-made direction detection Matlab code derived from Vromans and Giomi's method[50]. PIV measurements in Fig. 3a–c were obtained using confocal images in reflection mode. In this mode, the active nematic layer exhibits textures that can quite efficiently act as tracers for PIV software. The images were treated with ImageJ *PIV* plugin[52]. The data was then processed with custom Matlab codes. Flow profiles were computed using a custom ImageJ plugin. PIV measurements failed to give reliable measurements close to the walls for narrow channels because of a substantial drop of resolution that we attribute to artefacts in the reflection mode. Because of this, for a system in the shear flow state, the longitudinal velocity $V_x(y)$ was determined as follows. For each y position, a kymograph is built by assembling the image profile along the channel (x coordinate) at different times. The inhomogeneous reflected-light intensity results in traces in the $x-t$ plane of the kymograph, whose slope gives $V_x(y)$. The average value of this slope is obtained by computing the FFT of the kymograph image and finding at which angle the FFT has the highest intensity. We repeat the same process for each y coordinate, resulting in the desired flow profile. The kymograph in Fig. 3d was obtained with a custom Matlab code using PIV data from ImageJ as an input. Defect spacing in Fig. 2 was obtained by manually counting the number of defects in a given channel, for at least 10 random frames. Velocities were computed using ImageJ plugin Manual Tracking, averaging the velocities of 10 defects per experiment over their lifetime, typically 15 s.

Table 1 Composition of all stock solutions, and their volume fraction in the final mixture

Compound	Stock solution	v/V_{total}
PEG	12 % w.vol^{-1}	0.139
PEP	200 mM	0.139
High-salt M2B	69 mM $MgCl_2$	0.05
Trolox	20 mM	0.104
ATP	50 mM	0.03
Catalase	3.5 mg.ml^{-1}	0.012
Glucose	300 mg.ml^{-1}	0.012
Glucose Oxydase	20 mg.ml^{-1}	0.012
PK/LDH	600−1000 units.ml^{-1}	0.03
DTT	0.5 M	0.012
Streptavidin	0.352 mg.ml^{-1}	0.023
Kinesin	0.07 mg.ml^{-1}	0.234
Microtubules	6 mg.ml^{-1}	0.167
Pluronic	17%	0.027

Simulations. The Eqs. (1) and (2) of the manuscript are solved using a hybrid lattice–Boltzmann (LB) method. A finite difference scheme was used to solve Eq. (2) on a five-point stencil to discretize the derivatives on a square grid. These are coupled to Navier–Stokes equations, that are solved using lattice–Boltzmann method with the Bhatnagar–Gross–Krook (BGK) approximation and a single relaxation time for the collision operator[53]. The time integration is performed using PECE predictor–corrector method. The discrete space and time steps are chosen as unity for the LB method. The algorithm is implemented using the C++ programming language.

All simulations were performed on a $1800 \times w$ rectangular grid, where w varied from 30 to 160 lattice sites. The boundary conditions for the velocity field along all walls and corners are free-slip. The boundary conditions for the director field are weak planar along the channel walls, which is implemented via the free energy term $\frac{1}{2}W\mathrm{Tr}(\mathbf{Q}-\mathbf{Q}_\mathrm{D})^2$. The corners have $\mathbf{Q}_\mathrm{D}$ such that the director field aligns at an angle of 45 degrees to the length of the channel, on the front-right and back-left corners, and at an angle of 135 degrees on the front-left and back-right corners. The left and right walls have no free energy term applied, and have Neumann boundary conditions.

The parameters used in the simulations are given in Table 2. Initially, we chose parameters in a range that has previously been successful in reproducing the dynamics of experiments in microtubule bundles[54,55], and then further refined the parameters via a search in phase space. All simulations were run for up to 300,000 simulation time steps. Some simulations were performed up to 1,000,000 time steps to further test the stability of the simulations.

The initial velocity field was set to zero everywhere in the domain. The orientation of the director field was initialised at an angle of either 0, 35 or 90 degrees to the length of the channel, up to some noise. The noise was implemented using the uniform_real_distribution() function in the standard C++ library. In all simulations, the parameters were set to lattice units.

The figures of the simulations in Figs. 1 and 3a–c were created using the programme Paraview. In Fig. 1, the director field was overlaid on the order parameter field q. In Fig. 3a–c, the director field was overlaid on the vorticity field. The kymograph of the velocity components V_x and V_y in Fig. 3d, e was created using Matlab, by calculating the mean value of the velocity components in a subsection of the channel at any given time. The distributions of the defect

Table 2 Parameters used in the simulations

Parameter	Symbol	Value
Alignment parameter	ξ	0.9
Anchoring srength	W	0.002
Total density	ρ	40
Rotational diffusivity	Γ_Q	0.4
Elastic constant	K	0.015
Viscosity	η	1/6
Channel length	L_X	1800
Channel width	L_Y	30–160
Activity	ζ	0.0072–0.01

The values for ζ are 0.0072, 0.0075, 0.0082, 0.0092 and 0.01. All values are in LB units

positions across the channel width in simulations shown in Fig. 5 and Supplementary Fig. 5 were created using Matlab. Each bar represents the normalised number of defects along a strip of lattice sites parallel to the channel length, of width one lattice site. The supplementary movies of the simulations were created using Paraview, and any defect tracking was created by overlaying the Paraview images with markers from Matlab.

In the simulations, λ_i was calculated as follows. At any given channel width and time-step, the distance between each +1/2 defect and its nearest neighbour was calculated. The mean of this quantity was then taken, to give the mean defect-defect distance at a fixed time. Then an average over time was taken to give λ_i for a single simulation. This process was repeated for three different simulations with different initial conditions. The initial conditions were distinguished by the initialisation angle of the director field, which was selected to be 0, 45 and 90 degrees to the length of the channel. The mean value of these λ_i's was then taken to give the value plotted in Fig. 4. The standard deviation of these values were used to get the error bars.

Data availability

The data that support the findings of this study are available from the corresponding author upon reasonable request.

Code availability

Source data and codes for active nematic simulations are available from the corresponding author upon reasonable request.

Received: 4 March 2019; Accepted: 3 September 2019;
Published online: 04 October 2019

References

1. Ramaswamy, S. The mechanics and statistics of active matter. *Annl. Rev. Cond. Mat. Phys.* **1**, 323–345 (2010).
2. Marchetti, M. C. et al. Hydrodynamics of soft active matter. *Rev. Mod. Phys.* **85**, 1143–1189 (2013).
3. Friedl, P., Locker, J., Sahai, E. & Segall, J. E. Classifying collective cancer cell invasion. *Nat. Cell Biol.* **14**, 777–783 (2012).
4. Conrad, J. C. & Poling-Skutvik, R. Confined flow: Consequences and implications for bacteria and biofilms. *Annl. Rev. Chem. Biomol. Eng.* **9**, 175–200 (2018).
5. Wioland, H., Woodhouse, F. G., Dunkel, J., Kessler, J. O. & Goldstein, R. E. Confinement stabilizes a bacterial suspension into a spiral vortex. *Phys. Rev. Lett.* **110**, 268102 (2013).
6. Lushi, E., Wioland, H. & Goldstein, R. E. Fluid flows created by swimming bacteria drive self-organization in confined suspensions. *PNAS* **111**, 9733 (2014).
7. Wioland, H., Woodhouse, F. G., Dunkel, J. & Goldstein, R. E. Ferromagnetic and antiferromagnetic order in bacterial vortex lattices. *Nat. Phys.* **12**, 341–345 (2016).
8. Wioland, H., Lushi, E. & Goldstein, R. E. Directed collective motion of bacteria under channel confinement. *New J. Phys.* **18**, 075002 (2016).
9. Deforet, M., Hakim, V., Yevick, H., Duclos, G. & Silberzan, P. Emergence of collective modes and tri-dimensional structures from epithelial confinement. *Nat. Commun.* **5**, 3747 (2014).
10. Xi, W., Sonam, S., Beng Saw, T., Ladoux, B. & Teck Lim, C. Emergent patterns of collective cell migration under tubular confinement. *Nat. Commun.* **8**, 1517 (2017).
11. Duclos, G. et al. Spontaneous shear flow in confined cellular nematics. *Nat. Phys.* **14**, 728–732 (2018).
12. Duclos, G., Garcia, S., Yevick, H. G. & Silberzan, P. Perfect nematic order in confined monolayers of spindle-shaped cells. *Soft Matter* **10**, 2346–2353 (2014).
13. Duclos, G., Erlenkämper, C., Joanny, J. F. & Silberzan, P. Topological defects in confined populations of spindle-shaped cells. *Nat. Phys.* **13**, 58–62 (2017).
14. Guillamat, P., Ignés-Mullol, J. & Sagués, F. Taming active turbulence with patterned soft interfaces. *Nat. Commun.* **8**, 564 (2017).
15. Guillamat, P., Ignés-Mullol, J. & Sagués, F. Control of active nematics with passive liquid crystals. *Mol. Crys. Liq. Crys.* **646**, 226–234 (2017).
16. Guillamat, P., Hardoüin, J., Prat, B. M., Ignés-Mullol, J. & Sagués, F. Control of active turbulence through addressable soft interfaces. *J. Phys.: Cond. Mat.* **29**, 504003 (2017).
17. Opathalage, A. et al. Self-organized dynamics and the transition to turbulence of confined active nematics. *Proc. Natl Acad. Sci. USA* **116**, 4788–4797 (2019).
18. Keber, F. C. et al. Topology and dynamics of active nematic vesicles. *Science* **345**, 1135–1139 (2014).
19. Suzuki, K., Miyazaki, M., Takagi, J., Itabashi, T. & Ishiwata, S. Spatial confinement of active microtubule networks induces large-scale rotational cytoplasmic flow. *PNAS* **114**, 2922–2927 (2017).
20. Guillamat, P. et al. Active nematic emulsions. *Sci. Adv.* **4**, eaao1470 (2018).
21. Ellis, P. W. et al. Curvature-induced defect unbinding and dynamics in active nematic toroids. *Nat. Phys.* **14**, 85–90 (2018).
22. Wu, K. T. et al. Transition from turbulent to coherent flows in confined three-dimensional active fluids. *Science* **355**, 6331 (2017).
23. Ravnik, M. & Yeomans, J. M. Confined active nematic flow in cylindrical capillaries. *Phys. Rev. Lett.* **110**, 026001 (2013).
24. Whitfield, C. A., Marenduzzo, D., Voituriez, R. & Hawkins, R. J. Active polar fluid flow in finite droplets. *Eur. Phys. J. E* **37**, 8 (2014).
25. Giomi, L. & DeSimone, A. Spontaneous division and motility in active nematic droplets. *Phys. Rev. Lett.* **112**, 147802 (2014).
26. Sknepnek, R. & Henkes, S. Active swarms on a sphere. *Phys. Rev. E* **91**, 022306 (2015).
27. Zhang, R., Zhou, Y., Rahimi, M. & De Pablo, J. J. Dynamic structure of active nematic shells. *Nat. Commun.* **7**, 13483 (2016).
28. Alaimo, F., Köhler, C. & Voigt, A. Curvature controlled defect dynamics in topological active nematics. *Sci. Rep.* **7**, 5211 (2017).
29. Sanchez, T., Chen, D. T., DeCamp, S. J., Heymann, M. & Dogic, Z. Spontaneous motion in hierarchically assembled active matter. *Nature* **491**, 431–434 (2012).
30. Voituriez, R., Joanny, J. F. & Prost, J. Spontaneous flow transition in active polar gels. *Europhys. Lett.* **70**, 404–410 (2005).
31. Shendruk, T. N., Doostmohammadi, A., Thijssen, K. & Yeomans, J. M. Dancing disclinations in confined active nematics. *Soft Matter* **13**, 3853 (2017).
32. Guillamat, P., Ignés-Mullol, J., Shankar, S., Marchetti, M. C. & Sagués, F. Probing the shear viscosity of an active nematic film. *Phys. Rev. E* **94**, 060602 (2016).
33. Prost, J., Jülicher, F. & Joanny, J. F. Active gel physics. *Nat. Phys.* **11**, 111–117 (2015).
34. Doostmohammadi, A., Ignés-Mullol, J., Yeomans, J. M. & Sagués, F. Active nematics. *Nat. Commun.* **9**, 3246 (2018).
35. Beris, A. N. & Edwards, B. J. *Thermodynamics of Flowing Systems: With Internal Microstructure* (Oxford University Press, 1994).
36. Thampi, S. P., Doostmohammadi, A., Golestanian, R. & Yeomans, J. M. Intrinsic free energy in active nematics. *Europhys. Lett.* **112**, 28004 (2015).
37. Marenduzzo, D., Orlandini, E., Cates, M. E. & Yeomans, J. M. Steady-state hydrodynamic instabilities of active liquid crystals: Hybrid lattice Boltzmann simulations. *Phys. Rev. E* **76**, 031921 (2007).
38. Thampi, S. P., Golestanian, R. & Yeomans, J. M. Vorticity, defects and correlations in active turbulence. *Philos. Trans. A: Math. Phys. Eng. Sci.* **372**, 0366 (2014).
39. Giomi, L. Geometry and topology of turbulence in active nematics. *Phys. Rev. X* **5**, 031003 (2015).
40. Chaté, H., Ginelli, F. & Montagne, R. Simple model for active nematics: quasi-long-range order and giant fluctuations. *Phys. Rev. Lett.* **96**, 180602 (2006).
41. Ginelli, F., Peruani, F., Bär, M. & Chaté, H. Large-scale collective properties of self-propelled rods. *Phys. Rev. Lett.* **104**, 184502 (2010).
42. Simha, R. A. & Ramaswamy, S. Hydrodynamic fluctuations and instabilities in ordered suspensions of self-propelled particles. *Phys. Rev. Lett.* **89**, 058101 (2002).
43. Ramaswamy, S. & Rao, M. Active-filament hydrodynamics: instabilities, boundary conditions and rheology. *New J. Phys.* **9**, 423 (2007).
44. Guillamat, P., Ignés-Mullol, J. & Sagués, F. Control of active liquid crystals with a magnetic field. *PNAS* **113**, 5498–5502 (2016).

45. Pismen, L. M. Dynamics of defects in an active nematic layer. *Phys. Rev. E* **88**, 050502 (2013).
46. Denniston, C. Disclination dynamics in nematic liquid crystals. *Phys. Rev. B* **54**, 6272 (1996).
47. Norton, M. M. et al. Insensitivity of active nematic liquid crystal dynamics to topological constraints. *Phys. Rev. E* **97**, 012702 (2018).
48. Gao, T. & Li, Z. Self-driven droplet powered by active nematics. *Phys. Rev. Lett.* **119**, 108002 (2017).
49. DeCamp, S. J., Redner, G. S., Baskaran, A., Hagan, M. F. & Dogic, Z. Orientational order of motile defects in active nematics. *Nat. Matter* **14**, 1110–1115 (2015).
50. Vromans, A. J. & Giomi, L. Orientational properties of nematic disclinations. *Soft Matter* **12**, 6490–6495 (2016).
51. Srivastava, P., Mishra, P. & Marchetti, M. C. Negative stiffness and modulated states in active nematics. *Soft matter* **12**, 8214–8225 (2016).
52. Tseng, Q. et al. Spatial organization of the extracellular matrix regulates cell–cell junction positioning. *Proc. Natl. Acad. Sci.* **109**, 1506–1511 (2012).
53. Krüger, T. et al. The lattice Boltzmann method. *Springe. Int. Publ.* **10**, 978–3 (2017).
54. Melaugh, G. et al. Shaping the growth behaviour of biofilms initiated from bacterial aggregates. *PloS one* **11**, e0149683 (2016).
55. Lloyd, D. P. & Allen, R. J. Competition for space during bacterial colonization of a surface. *J. R. Soc. Interface* **12**, 20150608 (2015).
56. Loring, B., Karimabadi, H. & Rortershteyn, V. A screen space gpgpu surface lic algorithm for distributed memory data parallel sort last rendering infrastructures. Tech. Rep. (Lawrence Berkeley National Lab. (LBNL), Berkeley, CA, USA, 2014).

Acknowledgements

We are indebted to the Brandeis University Materials Research Science and Engineering Centers (MRSEC) Biosynthesis facility for providing the tubulin. We thank M. Pons, A. LeRoux, G. Iruela, P. Guillamat and B. Martínez-Prat (University of Barcelona) for assistance in the expression of motor proteins. We also thank P. Ellis and A. Fernandez-Nieves for kindly sharing all their image processing and defect detection algorithms. J.H., J.I.-M and F.S. acknowledge funding from Ministerio de Economia, Industria y Competitividad, Spain (project FIS2016-78507-C2-1-P, Agencia Estatal de Investigación/ European Regional Development Fund). J.H. acknowledges funding from the European Union's Horizon 2020 research and innovation program under grant agreement no. 674979- NANOTRANS. Brandeis University MRSEC Biosynthesis facility is supported by NSF MRSEC DMR-1420382. T.L-L. acknowledges funding from the French Agence Nationale de la Recherche (Ref. ANR-13-JS08-006-01). Gulliver laboratory acknowledges funding from 2015 Grant SESAME MILAMIFAB (Ref. 15013105) for the acquisiton of a Nanoscribe GT Photonic Professional device. R.H. acknowledges that this research was supported by the European Union's Horizon 2020 research and innovation programme under the Marie Sklodowska-Curie grant agreement No 722497 - LubISS.

Author contributions

J.H., J.L., F.S. and J.I.-M. conceived the experiments and R.H., A.D. and J.M.Y. designed the simulations. J.H. performed the experiments in collaboration with T.L.-L. and analyzed the experimental data. R.H. conducted the numerical simulations. J.H., R.H. and J.M.Y. wrote the paper with contribution from all the authors.

Competing interests

The authors declare no competing interests.

Additional information

Supplementary information is available for this paper at https://doi.org/10.1038/s42005-019-0221-x.

Correspondence and requests for materials should be addressed to J.M.Y. or J.-M.

Reprints and permission information is available at http://www.nature.com/reprints

Publisher's note Springer Nature remains neutral with regard to jurisdictional claims in published maps and institutional affiliations.